A&A 654, A32 (2021)
https://doi.org/10.1051/0004-6361/202141474

Astronomy & Astrophysics

X-ray obscuration from a variable ionized absorber in PG 1114+445

R. Serafinelli[1], V. Braito[1,2], P. Severgnini[1], F. Tombesi[3,4,5,6], G. Giani[1,7], E. Piconcelli[6], R. Della Ceca[1], F. Vagnetti[3,8], M. Gaspari[9,10], F. G. Saturni[6,11], R. Middei[6,11], and A. Tortosa[12]

[1] INAF – Osservatorio Astronomico di Brera, Via Brera 28, 20121, Milano; Via Bianchi 46, 23807 Merate (LC), Italy
e-mail: roberto.serafinelli@inaf.it
[2] Department of Physics, Institute for Astrophysics and Computational Sciences, The Catholic University of America, Washington, DC 20064, USA
[3] Dipartimento di Fisica, Università degli Studi di Roma "Tor Vergata", Via della Ricerca Scientifica 1, 00133 Roma, Italy
[4] X-ray Astrophysics Laboratory, NASA/Goddard Space Flight Center, Greenbelt, MD 20771, USA
[5] Department of Astronomy, University of Maryland, College Park, MD 20742, USA
[6] INAF – Osservatorio Astronomico di Roma, Via Frascati 33, 00044 Monte Porzio Catone, Roma, Italy
[7] Dipartimento di Fisica, Università degli Studi di Milano, Via Celoria, 16, 20133 Milano, Italy
[8] INAF – Istituto di Astrofisica e Planetologia Spaziali, Via del Fosso del Cavaliere 100, 00133 Roma, Italy
[9] INAF, Osservatorio di Astrofisica e Scienza dello Spazio, via P. Gobetti 93/3, 40129 Bologna, Italy
[10] Department of Astrophysical Sciences, Princeton University, Princeton, NJ 08544, USA
[11] Space Science Data Center, Agenzia Spaziale Italiana, Via del Politecnico snc, 00133 Roma, Italy
[12] Núcleo de Astronomía de la Facultad de Ingeniería, Universitad Diego Portales, Av. Ejército Libertador 441, Santiago, Chile

Received 4 June 2021 / Accepted 13 July 2021

ABSTRACT

Photoionized absorbers of outflowing gas are commonly found in the X-ray spectra of active galactic nuclei. While most of these absorbers are seldom significantly variable, some ionized obscurers have increasingly been found to substantially change their column density on a wide range of timescales. These $N_{\rm H}$ variations are often considered as the signature of the clumpy nature of the absorbers. Here we present the analysis of a new *Neil Gehrels Swift* Observatory campaign of the type 1 quasar PG 1114+445, which was observed to investigate the time evolution of the multiphase outflowing absorbers previously detected in its spectra. The analyzed dataset consists of 22 observations with a total exposure of ∼90 ks that spans about 20 months. For the whole campaign, we report an unusually low flux state with respect to all previous X-ray observations of this quasar. From the analysis of the stacked spectra, we find a fully covering absorber with a column density $\log(N_{\rm H}/{\rm cm}^{-2}) = 22.9^{+0.3}_{-0.1}$. This is an order of magnitude higher than the column density measured in the previous observations. This is either due to a variation of the known absorbers or to a new one that eclipses the X-ray emitting source. We also find an ionization parameter of $\log(\xi/{\rm erg\,cm\,s^{-1}}) = 1.4^{+0.6}_{-0.2}$. Assuming that the obscuration lasts for the whole duration of the campaign, that is, more than 20 months, we estimate the minimum distance of the ionized clump, which is located at $r \gtrsim 0.5$ pc.

Key words. X-rays: galaxies – galaxies: active – quasars: general – quasars: individual: PG 1114+445

1. Introduction

Active galactic nuclei (AGN) are extremely luminous extragalactic objects that are located at the center of their host galaxies and are powered by the accretion of matter onto a supermassive black hole (SMBH). AGN are now considered a major force in shaping their host galaxy during its evolution because many of the galaxy properties are correlated with the mass of the central SMBH (e.g., Ferrarese & Merritt 2000; Häring & Rix 2004; Gaspari et al. 2019). Outflows are one of the main mechanisms by which the black hole is thought to transport its energy to large distances (e.g., King & Pounds 2015; Fiore et al. 2017; Cicone et al. 2018; Laha et al. 2021). These winds are commonly found at many wavelengths in AGN spectra (e.g., Gibson et al. 2009; Harrison et al. 2014; Cicone et al. 2014; Vietri et al. 2018).

In the X-ray band, absorption features are the typical signature of outflows. Low-ionization absorbers ($\log(\xi/{\rm erg\,cm\,s^{-1}}) \lesssim 2$), characterized by a low outflow velocity ($v_{\rm out} \sim 100-1000\,{\rm km\,s^{-1}}$), are found in about 65% of the soft X-ray ($E \lesssim 2\,{\rm keV}$) spectra of nearby AGN, and they are often known as warm absorbers (WAs, e.g., Halpern 1984; Blustin et al. 2005; McKernan et al. 2007; Laha et al. 2014). More than 30% of the X-ray detected AGN show evidence of ultra-fast outflows (UFOs, e.g., Chartas et al. 2002; Pounds et al. 2003a,b; Braito et al. 2007; Tombesi et al. 2010, 2015; Gofford et al. 2013; Nardini et al. 2015; Ballo et al. 2015). UFOs are extremely highly ionized ($\log(\xi/{\rm erg\,cm\,s^{-1}}) \sim 3-6$) absorbers that are detected as blueshifted absorption lines of Fe XXV and XXVI, with typical outflow velocity of $v_{\rm out} \sim 0.1c$, but are capable of reaching near-relativistic values of $\sim 0.5c$ (e.g., Reeves et al. 2018; Luminari et al. 2021).

While UFOs are extremely variable (e.g., Matzeu et al. 2017), variability of soft X-ray ionized absorbers is found less frequently. In some cases, some sources are found in a state with diminished X-ray flux due to an increase in column density of the obscuring medium. The absorbers are sometimes found to be persistent for about a decade (e.g., NGC 5548, Kaastra et al. 2014). In other cases, the obscurer has a much shorter variability timescale (e.g., Severgnini et al. 2015; Matzeu et al. 2016; Mehdipour et al. 2017; Middei et al. 2020).

In a few other cases, a source was found in a higher flux state than usual because of a diminished obscuring power of the WA (e.g., Braito et al. 2014). All these cases suggest a clumpy structure for the ionized and possibly outflowing absorbers around the AGN, which is predicted by duty-cycle theoretical models such as chaotic cold accretion (CCA, e.g., Gaspari et al. 2013; Gaspari & Sądowski 2017). This clumpy material can be part of the multiphase rain condensing out of the hot halo, which then eventually contributes to the feeding component alongside the feedback channel. Feeding and feedback processes are indeed expected to be tightly self-regulated over cosmic time and over nine orders of magnitude in spatial scale (see, e.g., Gaspari et al. 2020, for a review).

The type 1 quasar PG 1114+445 ($z = 0.144$, Hewett & Wild 2010) has an estimated black hole mass of $\log(M/M_\odot) \simeq 8.8$ and bolometric luminosity of $\log(L_{\rm bol}/{\rm erg\,s^{-1}}) \simeq 45.7$ (Shen et al. 2011). This means that the source is accreting with an Eddington ratio of $\log(L_{\rm bol}/L_{\rm Edd}) \simeq -1.14$. The source is well known to host multiple absorbers in the UV and X-ray bands. An UV observation taken in 1996 with the Faint Object Spectrograph (FOS) on board the *Hubble* Space Telescope (HST) was able to detect Lyα and C IV absorption lines in the spectrum of this quasar. For these lines, an outflowing velocity of $\sim$530 km s^{-1} was measured (Mathur et al. 1998). The observation was simultaneous with an Advance Satellite for Cosmology and Astrophysics (ASCA) pointing that highlighted an ionized WA and showed marginal evidence of an absorption line at $E \sim 7.3$ keV (George et al. 1997). The UV absorption lines and the X-ray warm absorber have similar ionizations and therefore they likely trace the same material (Mathur et al. 1998).

The source was again observed in 2002 with *XMM-Newton* (Jansen et al. 2001), revealing that the absorption complex consisted of two WA layers (Ashton et al. 2004; Piconcelli et al. 2005). A further *XMM-Newton* campaign of 11 observations was performed in 2010. The data from this campaign, together with a reanalysis of the 2002 observation (Serafinelli et al. 2019, hereafter Paper I), found that one of the two absorbers has typical WA parameters, that is, column density $N_{\rm H} \simeq 7.6 \times 10^{21}$ cm^{-2} and ionization parameter $\log(\xi/{\rm erg\,cm\,s^{-1}}) \simeq 0.35$ with velocity below the energy resolution, that are likely associated with the UV absorber (Mathur et al. 1998). The second absorber shares very similar parameters with the WA ($N_{\rm H} \sim 3 \times 10^{21}$ cm^{-2} and $\log(\xi/{\rm erg\,cm\,s^{-1}}) \sim 0.5$), with the exception of the outflow velocity, which is high enough to be detected with the EPIC cameras on board *XMM-Newton* ($v_{\rm out}/c = 0.12 \pm 0.03$). Low-ionization fast outflows were also found in other sources (e.g., Longinotti et al. 2015; Pounds et al. 2016; Reeves et al. 2020). In addition, a high-ionization UFO ($v_{\rm out}/c = 0.15 \pm 0.04$, consistent with the fast absorber) was found in three spectra. This evidence led to the interpretation that a UFO pushes and entrains the interstellar medium of the host galaxy to a comparable velocity, producing a so-called entrained ultra-fast outflow (E-UFO, Paper I).

We analyze the data taken during a recent *Neil Gehrels Swift* Observatory (hereafter *Swift*) X-Ray Telescope (XRT, Gehrels et al. 2004) campaign, which was proposed to study the possible variability of the absorbers found in Paper I, on timescales from days to months. In Sect. 2 we describe how the data were prepared for the analysis. In Sect. 3 we analyze the X-ray amplitude and spectral variability, and in Sect. 4 we present detailed spectroscopy of the source. In Sect. 5 we analyze the variability of the X-ray-to-UV ratio. We summarize and discuss our results in Sect. 6.

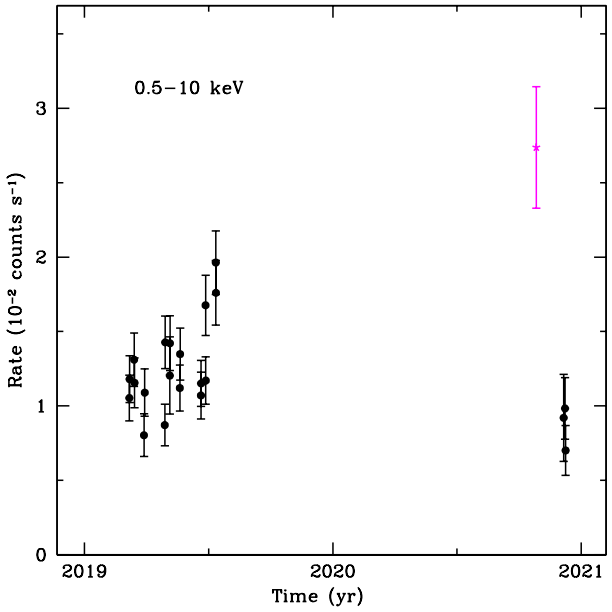

Fig. 1. *Swift*-XRT count rates in the energy band $E = 0.5-10$ keV. The magenta star represents OBSID 00089058001, which was not part of our campaign.

Throughout the paper, we adopt the following cosmology: $\Omega_m = 0.3$, $\Omega_\Lambda = 0.7$, and $H_0 = 70$ km s^{-1} Mpc^{-1}. All uncertainties are reported at a 90% confidence level.

2. Observations and data reduction

The observations were performed during *Swift* Cycle 15 (PI: Serafinelli) from March to July 2019 (OBSID 00011004001 to 00011004018), and then three additional observations were taken 15 months later, in December 2020 (OBSID 00011004019 to 00011004021). The observations were spaced by 7, 15, and 30 days in order to analyze possible short-time variability within the campaign. A further archival observation, OBSID 00089058001, not part of our campaign, taken on October 26, 2020, is also considered here. Most observations are about $\sim$4−5 ks long, and some observations are only $\sim$2 ks long. The list of *Swift*-XRT observations is shown in Table 1. The total exposure time is $\sim$90 ks.

For each *Swift*-XRT observation, the source and background spectra were extracted using the HEASOFT task XSELECT. The source spectrum was extracted from a circular area of 40″ radius around the object, while the background spectrum was extracted from two source-free circular areas of 40″ radius each in the proximity of the source. Ancillary files were produced using the XRTMKARF task, while the response was taken from the HEASOFT CALDB repository.

Each *Swift* observation provided an UltraViolet and Optical Telescope (UVOT) pointing, with a single filter, centered on the source. The source monochromatic flux was measured within circular apertures of 5″ radius, while the background was extracted from an annulus region, centered on the source, with an internal radius of 15″ and an external radius of 40″ using the UVOTSOURCE task.

3. X-ray variability

The *Swift*-XRT count rate light curve of PG 1114+445 in the 0.5−10 keV full band is shown in Fig. 1. The average count rate is $\sim 1.5 \times 10^{-2}$ cts s^{-1}. We compare the current data

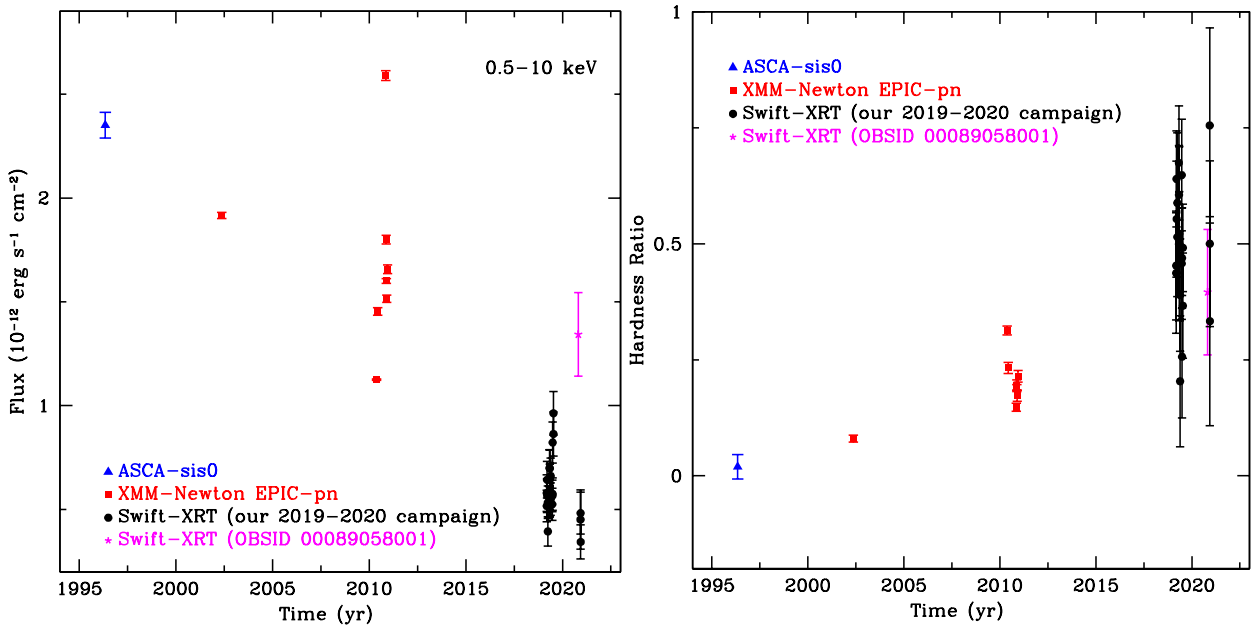

Fig. 2. Full-band (E = 0.5−10 keV) light curve using ASCA data (blue triangle), *XMM-Newton* (red squares), our *Swift*-XRT campaign (black circles), and additional archival *Swift*-XRT observation (magenta star; *left*). Time variability of the hardness ratio HR = $(H - S)/(H + S)$, where S and H are the 0.5−2 and 2−10 keV count rates, respectively (*left*). The spectrum in the most recent data is noticeably harder. The count rates of the ASCA and EPIC-pn observations were converted into *Swift*-XRT count rates following the procedure described in Sect. 3.

Table 1. X-ray observations taken by *Swift*-XRT, with OBSID, observation date, and exposure.

Observation ID	Date	Exposure (s)
00011004001	2019-03-08	4909
00011004002	2019-03-08	4978
00011004003	2019-03-15	4258
00011004004	2019-03-15	4475
00011004005	2019-03-29	4249
00011004006	2019-03-30	4750
00011004007	2019-04-29	4957
00011004008	2019-04-29	4821
00011004009	2019-05-06	4313
00011004010	2019-05-06	1920
00011004011	2019-05-21	5152
00011004012	2019-05-21	4874
00011004013	2019-06-21	5070
00011004014	2019-06-21	5151
00011004015	2019-06-28	4404
00011004016	2019-06-28	4849
00011004017	2019-07-13	4051
00011004018	2019-07-13	4527
00089058001	2020-10-26	1804
00011004019	2020-12-06	1855
00011004020	2020-12-08	2453
00011004021	2020-12-08	2795

set with archival X-ray pointings from ASCA, taken in 1996 and *XMM-Newton*, taken in 2002 and 2010. The products of the ASCA observation were downloaded from the Tartarus database[1] (Turner et al. 2001), while details of the *XMM-Newton* data reduction can be found in Paper I. In order to compare data taken with different telescopes, we converted the X-ray count rates into fluxes. All fluxes were obtained with the web tool WebPIMMS[2], adopting a simple AGN X-ray spectrum, composed of a typical $\Gamma = 1.9$ power law (e.g., Corral et al. 2011; Serafinelli et al. 2017), at the redshift of the source (z = 0.144), with Galactic absorption ($N_{\rm H,Gal} = 1.87 \times 10^{20}$ cm^{-2}, HI4PI Collaboration 2016). The full band fluxes as a function of the observation time are plotted in the left panel of Fig. 2, where an evident decrease in X-ray flux can already be identified by eye.

The possible presence of obscuration can be investigated by the use of the hardness ratio (HR), which we define as $(H - S)/(H + S)$, where S is the count rate in the soft band (E = 0.5−2 keV) and H is the count rate in the hard band (E = 2−10 keV). In order to deal with comparable HRs, which are typically different due to the different responses of the instruments, we converted all the count rates into those of *Swift*-XRT using WebPIMMS and again assuming a simple absorbed $\Gamma = 1.9$ power law at $z = 0.144$, with $N_{\rm H,Gal} = 1.87 \times 10^{20}$ cm^{-2}. As shown in Fig. 2 (right panel), the spectrum in the *Swift*-XRT observations hardens on average, whereas the HR values during the whole *Swift*-XRT campaign remain approximately consistent within the error bars. During the observation performed on 26 October 2020, that is, the magenta point in Figs. 1 and 2, the flux was higher than during the remainder of the 2019-2020 campaign. However, the HR is still consistent with the value of the other observations of the *Swift* campaign. That the HR is higher than in the *XMM-Newton* observations suggests that the lower flux state is not due to a change in the primary continuum, but likely to a variation of the column density of one or more of the known absorbers found in Paper I.

[1] https://heasarc.gsfc.nasa.gov/FTP/asca/data/tartarus/products/74072000/74072000_gsfc.html

[2] https://heasarc.gsfc.nasa.gov/cgi-bin/Tools/w3pimms/w3pimms.pl

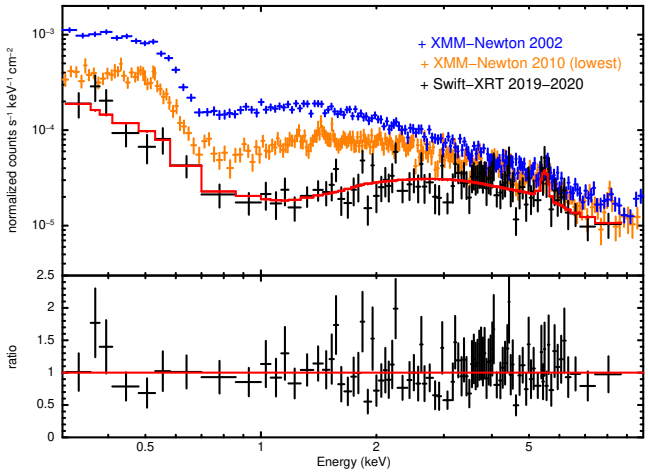

Fig. 3. Composite *Swift*-XRT spectrum (black) with its best-fit model (*upper panel*) and data-to-model ratios (*lower panel*). For comparison, we also show the 2002 EPIC-pn observation (blue) and the lowest-flux spectrum of the 2010 campaign (orange).

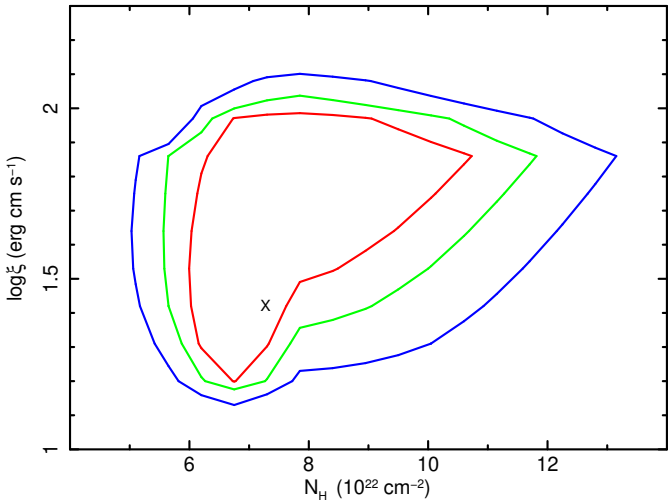

Fig. 4. Contour plot for the ionization $\log \xi$ and the column density $N_{\rm H}$. The red line represents the 1σ confidence level (68%), and the green and blue lines represent the 2σ (95%) and 3σ (99.7%) confidence levels. The cross marks the best-fit values.

4. X-ray spectral analysis

Because all *Swift*-XRT observations have only a few photon counts, we combined all the observations into a single spectrum using the HEASOFT task ADDSPEC in order to maximize the signal-to-noise ratio. We binned the combined spectrum, which consists of ∼1300 net counts, to have at least ten counts per energy channel.

All spectral fits were performed using XSPEC v12.10 (Arnaud 1996), adopting a C-statistic, because of the low number of photons for each bin (e.g., Kaastra 2017). We first attempted to fit the combined spectrum with a simple model consisting of a power-law component and an emission line, with Galactic absorption characterized by a fixed column density $N_{\rm H,Gal} = 1.87 \times 10^{20}\,{\rm cm}^{-2}$ (HI4PI Collaboration 2016): `Tbabs × (powerlaw + zgauss)`. The fit results in an unacceptable C-statistic: $C/{\rm d.o.f.} = 229/106$, where d.o.f. is the degree of freedom, and an unrealistic photon index, $\Gamma = 0.4 \pm 0.1$.

Based on previous analyses of PG 1114+445 (George et al. 1997; Ashton et al. 2004; Piconcelli et al. 2005, Paper I), we included an ionized absorber using a partial covering model, ZXIPCF (Reeves et al. 2008). The assumed model is therefore `Tbabs × zxipcf × (powerlaw + zgauss)`. The addition of this ionized absorption component significantly improved the goodness of fit, with a C-stat of $C/{\rm d.o.f.} = 106/103$. The best-fit value found for the photon index is $\Gamma = 1.6^{+0.3}_{-0.4}$, which is consistent with the values measured in Paper I. We find that the absorber is moderately ionized, $\log(\xi/{\rm erg\,cm\,s^{-1}}) = 1.4^{+0.6}_{-0.2}$, and almost fully covering, with a covering factor $C_f = 0.96^{+0.03}_{-0.07}$, with a column density of $N_{\rm H} = 7^{+5}_{-1} \times 10^{22}\,{\rm cm}^{-2}$. This value is a factor of ∼10 higher than the column density of any low-ionization absorber detected in Paper I, which confirms that the flux decrease is mainly due to a column density increase with respect to the 2010 observations. The spectrum, the best-fit model, and the data-to-model residuals are shown in Fig. 3. The best-fit values are summarized in Table 2. The confidence contour plot of the joint errors of the ionization parameter versus $N_{\rm H}$ is shown in Fig. 4. In particular, the column density is higher than the $N_{\rm H}$ of any soft X-ray absorber detected in Paper I at the 3σ confidence level.

Table 2. Summary of the best-fit parameters for our best model: `TBabs × zxipcf × (powerlaw + zgauss)`.

Parameter	Value
$\log N_{\rm H}$ (cm^{-2})	$22.9^{+0.3}_{-0.1}$
$\log \xi$ (erg cm s^{-1})	$1.4^{+0.6}_{-0.2}$
C_f	$0.96^{+0.03}_{-0.07}$
Γ	$1.6^{+0.3}_{-0.4}$
norm (cts s^{-1})	$3.1^{+2.2}_{-1.4} \times 10^{-4}$
$E_{{\rm K}\alpha}$ (keV)	6.28 ± 0.08
norm$_{{\rm K}\alpha}$ (cts s^{-1})	$7^{+4}_{-3} \times 10^{-6}$
Cstat/d.o.f.	106/103

Notes. Errors are given at the 90% confidence level.

5. UV variability

The UV observations were provided by the *XMM-Newton* Optical Monitor (OM) and by *Swift*-UVOT. The OM data were retrieved from the XMM Serendipitous Ultraviolet Source Survey (XMM-SUSS, Page et al. 2012). None of the UVOT filters show evidence of relevant variability between 2010 and 2019-2020 (see Table 3).

We computed the X-ray/UV ratio $\alpha_{\rm ox}$ (e.g., Vignali et al. 2003; Vagnetti et al. 2010; Lusso & Risaliti 2016; Chiaraluce et al. 2018) in order to analyze the relative variability of the X-ray and UV bands, which is defined as

$$\alpha_{\rm ox} = \frac{\log L(2\,{\rm keV}) - \log L(2500\,{\rm \AA})}{\log \nu(2\,{\rm keV}) - \log \nu(2500\,{\rm \AA})},$$

where $\nu(2\,{\rm keV})$ and $\nu(2500\,{\rm \AA})$ are the frequencies (in Hz) in the rest frame, corresponding to an energy of 2 keV and a wavelength of 2500 Å, respectively. The 2 keV luminosity of the XRT observations was computed using XSPEC. We adopted the best-fit model (see Sect. 4) and froze every parameter with the exception of the column density $N_{\rm H}$ of the absorber and the normalization of the power law. We fit each snapshot with this model to obtain a best-fit model as accurate as possible, and

Table 3. Flux densities in units of 10^{-15} erg cm^{-2} s^{-1} Å^{-1} for each *Swift*-UVOT pointing.

OBSID	UV filter	Flux (10^{-15} erg cm^{-2} s^{-1} Å^{-1})
00011004001	UVM2	4.19 ± 0.07
00011004002	UVW2	5.01 ± 0.07
00011004003	UVM2	4.39 ± 0.07
00011004004	UVW2	4.82 ± 0.07
00011004005	UVM2	4.38 ± 0.07
00011004006	UVW2	5.18 ± 0.08
00011004007	UVM2	3.92 ± 0.06
00011004008	UVW2	4.58 ± 0.07
00011004009	UVM2	3.92 ± 0.06
00011004010	UVW2	4.42 ± 0.08
00011004011	UVM2	3.91 ± 0.06
00011004012	UVW2	4.39 ± 0.07
00011004013	UVM2	4.06 ± 0.07
00011004014	UVW2	4.95 ± 0.07
00011004015	UVM2	4.35 ± 0.07
00011004016	UVW2	5.13 ± 0.08
00011004017	UVM2	4.17 ± 0.07
00011004018	UVW2	4.96 ± 0.07
00089058001	U	3.68 ± 0.06
00011004019	UVW2	5.78 ± 0.10
00011004020	UVW1	4.67 ± 0.08
00011004021	U	3.83 ± 0.06

Notes. The corresponding UVOT filter is also reported.

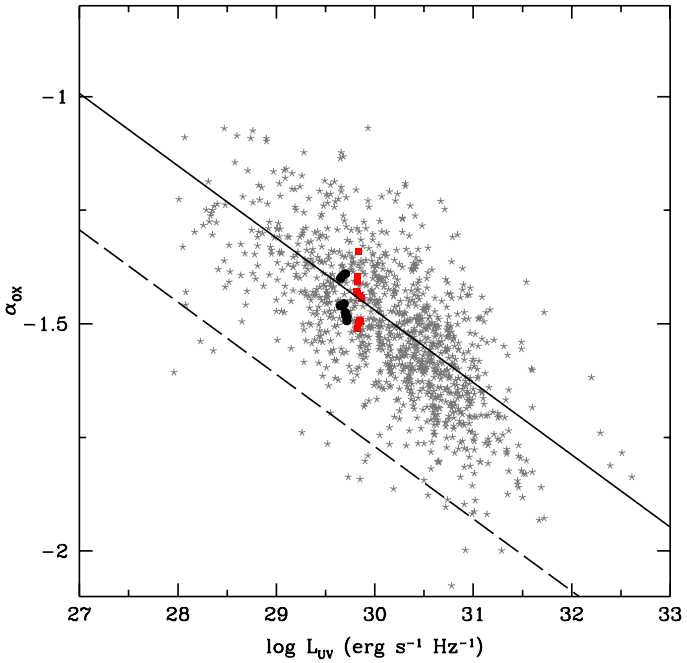

Fig. 5. Plot of the α_{ox} index vs. the UV luminosity using unabsorbed X-ray luminosities. The gray points are the quasars analyzed in Chiaraluce et al. (2018). The linear best fit is shown as a solid line. The dashed line is the X-ray weak limit defined by Pu et al. (2020). The red squares correspond to the *XMM-Newton* observations, and the black points correspond to those performed by *Swift*.

then we removed the absorption component and used the LUMIN task between 1.99 and 2.01 keV, from which we derived the intrinsic X-ray luminosity L(2 keV). Because the UVOT observations were performed with a single source-centered filter, we computed the luminosity at 2500 Å by interpolating a spectral energy distribution obtained by averaging thousands of Sloan Digital Sky Survey (SDSS) observations (Richards et al. 2006). We conservatively computed L(2500 Å) only for the observations performed with the UVM2 filter, which is centered at ∼2250 Å, corresponding to a rest-frame wavelength of ∼2510 Å, and therefore close enough to 2500 Å. The fluxes were finally corrected for reddening due to the Galactic extinction adopting $E(B-V) = 0.0264$ (Güver & Özel 2009).

The result is shown in Fig. 5. The *Swift* observations lie on the general trend found by Chiaraluce et al. (2018), which is represented by a solid line. We note that none of the points lie on the X-ray weak limit (dashed line), which is set 0.3 dex below the best-fit line (Pu et al. 2020). This is further proof that the low flux state of the source is clearly driven by the obscuration and not by an intrinsic luminosity change.

6. Summary and discussion

We have presented the analysis of the *Swift* observations of the type 1 quasar PG 1114+445, performed ten years after the *XMM-Newton* observations analyzed in Paper I. The source is found in a strongly reduced flux state (Fig. 2), which can be ascribed to an absorption increase caused by an obscuring material. The spectral analysis highlights the presence of ionized ($\log \xi$/erg cm s^{-1} ∼ 1.4) material, characterized by a column density $N_H \sim 7 \times 10^{22}$ cm^{-2}. No substantial variations in the unabsorbed X-ray luminosity of the source were found.

In Paper I, two absorbers were found in the soft X-rays, a slow and constant WA with $N_H \sim 7 \times 10^{21}$ cm^{-2}, and a mildly relativistic absorber, identified with an E-UFO, with a variable column density with a median value $N_H \sim 3 \times 10^{21}$ cm^{-2} and a dispersion of $\sim 6 \times 10^{20}$ cm^{-2}. Both these column densities are a factor of 10 lower than the density found in this work. If we allow for an outflowing velocity of this ionized absorber, we obtain that the best-fit value of the redshift of the absorber in the observer frame is $z_{obs} \sim 0.09$, which corresponds to $v_{out} \sim 0.05c$. However, the low statistics of the dataset does not allow us to successfully measure both the ionization parameter and the velocity, which are notoriously affected by degeneracy, as shown by their contour plot in Fig. 6. We note that lower values of the absorber redshift are allowed at the 1σ confidence level, down to $z_{obs} \simeq -0.03$ ($v_{out} \simeq 0.16c$), consistent with both the E-UFO and the WA measured in Paper I. In addition, the ionization parameter can be as low as $\log \xi \lesssim 0.4$ at the 3σ confidence level, consistent with the E-UFO median value of 2010. This suggests that *Swift*-XRT is not able to resolve the complex structure of the absorbers measured in Paper I, but it may be hidden by the dominant absorber that we observe in this campaign.

We can estimate a lower limit for its distance using the equation by Risaliti et al. (2002),

$$r \simeq 4 \times 10^{16} \frac{M_{BH}}{10^{M}_{\odot}} \left(\frac{n}{10^{9}\ \mathrm{cm}^{-3}} \frac{t}{1\ \mathrm{day}} \frac{N_H}{5 \times 10^{22}\ \mathrm{cm}^{-2}} \right)^{2} \mathrm{cm} \simeq 2 \times 10^{23} n_9^2\ \mathrm{cm}, \quad (1)$$

where $M_{BH} \simeq 6.3{\times}10^{8}\ M_{\odot}$ is the black hole mass, n is the density of the clump (n_9 in units of 10^9 cm^{-3}), $N_H \simeq 7 \times 10^{22}$ cm^{-2} is the column density of the clump, and t is the duration of the obscuration. We assume here that the obscuration lasts for the whole campaing, including the times between 2019 and 2020

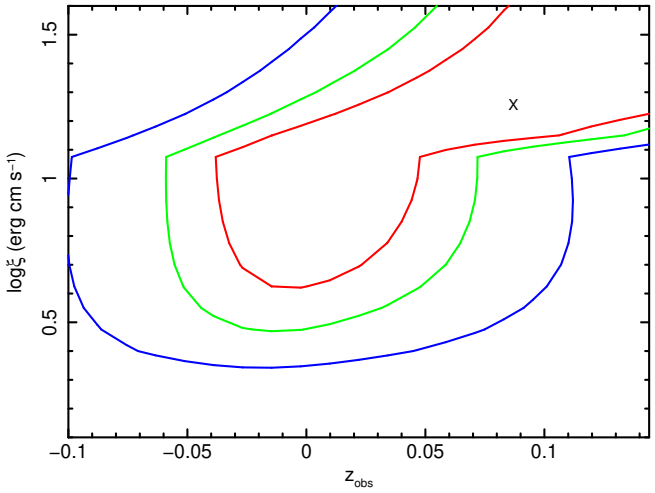

Fig. 6. Contour plots between the redshift of the absorber in the observer frame z_{obs} and the ionization parameter $\log \xi$. The red, green, and blue line represent the 1σ (68%), 2σ (95%) and 3σ (99.7%) confidence levels, respectively.

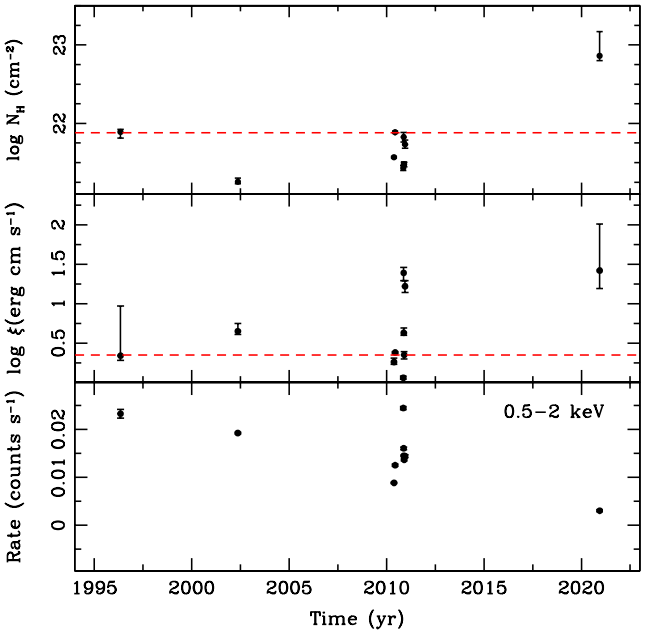

Fig. 7. Time variability of the absorber parameters N_H (*top*) and ξ (*middle*). For all observations prior to 2019, the black points refer to the variable E-UFO, while the constant WA is represented by the dashed red line. In the *lower panel*, the light curve of soft X-ray ($E = 0.5-2$ keV) count rates is shown, where the XMM rates were converted into *Swift*-XRT count rates using WebPIMMS.

when the source was not observed. Therefore we adopt $t \gtrsim 560$ days (rest-frame) as the duration of the obscuration, which is only a lower limit because it might last beyond the end of the campaign. The density of the clump can be replaced by inverting the definition of the ionization parameter,

$$n = \frac{L_{\rm ion}}{r^2 \xi}, \tag{2}$$

where $L_{\rm ion} \simeq 1.5 \times 10^{44}$ erg s^{-1} is obtained from the unabsorbed best-fit model, and $\xi = 25^{+35}_{-11}$ erg cm s^{-1} is the best-fit value (see Table 2). Combining Eqs. (1) and (2), we obtain an upper limit for the density of the obscuring clump $n = (2.7 \pm 0.5) \times 10^6$ cm^{-3}, which means that it is located at least at $r = (1.5 \pm 0.5) \times 10^{18}$ cm $= (0.50 \pm 0.15)$ pc $= (8 \pm 2) \times 10^3 r_s$, where $r_s = 2GM/c^2$ is the Schwarzschild radius. The estimated minimum size of the clump is therefore $R \simeq N_{\rm H}/n = (6 \pm 2) \times 10^{-3}$ pc.

An estimate of the maximum distance of the cloud from the central source might be given by noting that the size of the clump cannot be larger than its distance from the X-ray source. Therefore we assume $N_{\rm H} = nR < nr_{\rm max}$ (e.g., Crenshaw & Kraemer 2012; Tombesi et al. 2013). Substituting this into the definition of ionization parameter, we obtain

$$r_{\rm max} = \frac{L_{\rm ion}}{N_{\rm H} \xi}. \tag{3}$$

Assuming again $L_{\rm ion} \simeq 1.5 \times 10^{44}$ erg s^{-1}, and the best-fit values of $N_{\rm H}$ and ξ (Table 2), we obtain $r_{\rm max} = 30^{+40}_{-13}$ pc $= 5^{+5}_{-2} \times 10^5$ r_s.

The increase in column density is likely due to a new clump of absorbing material, either due to a superposition of the WA and the E-UFO observed in Paper I, with an increased column density $N_{\rm H}$, or an additional absorber located between the central source and the previously known absorber. The values of the minimum and maximum distance of the clump found in Eqs. (1) and (3) strongly suggest that the absorbing clumps are located outside the typical boundaries of the broad line region for a quasar of this luminosity. We estimate a broad line region radius of $R_{\rm BLR} \simeq 0.07$ pc, considering the luminosity $\log(L_{5100\text{Å}}/\text{erg s}^{-1}) \simeq 44.77$ of PG 1114+445 (Shen et al. 2011), when the relation between $R_{\rm BLR}$ and $L_{5100\text{Å}}$ derived by Bentz et al. (2009) is assumed. A comparison between the parameters of the absorber detected here and those measured in Paper I is shown in Fig. 7.

While no strong flux variability is detected between the *Swift*-XRT observations, minor variations are present (Figs. 1 and 2) and may be tied to the observed increased clumpiness. For instance, CCA predicts fractal variations with a power spectral density proportional to f^{-1}, where f is the time frequency. In other words, smaller clumps are expected to contribute to the micro variations observed in the light curves (e.g., Gaspari et al. 2017). The distance estimate places the cloud at the meso scale in the CCA self-regulation framework (Gaspari et al. 2020). This is the typical transition scale at which CCA clouds become more clustered and collide frequently, thus generating flickering absorbers along the line of sight, starting from the X-ray/hot phase and potentially down to the radio/molecular phase (e.g., Tremblay et al. 2018; Rose et al. 2019).

In the past decade, many obscuring variable absorbers were found in the X-ray spectra of nearby AGN (e.g., Markowitz et al. 2014), with timescales ranging from decades (e.g., Kaastra et al. 2014) to months or weeks (e.g., Matzeu et al. 2016; Mehdipour et al. 2017; Middei et al. 2020) and even days (e.g., Braito et al. 2014; Severgnini et al. 2015). These winds, with velocities than can be higher than typical WA velocities, are important because they may carry sufficient kinetic power to contribute to possible AGN feedback on the host galaxy. It is therefore important to continue monitoring these sources and possibly several others with current facilities such as *Swift* or eROSITA (Merloni et al. 2012), and with future missions such as the enhanced X-ray Timing and Polarimetry mission (eXTP, Zhang et al. 2019), XRISM/Xtend (e.g., Yoneyama et al. 2020), or the *Athena* Wide Field Imager (WFI, Meidinger et al. 2015) in order to search for both long-term and transient obscuration from ionized clumps. In the case of PG 1114+445, given the long-term nature of its obscuration, a monthly monitoring could

help to identify lowest and highest states, to study them with current X-ray telescopes such as *XMM-Newton*. In the future, forthcoming microcalorimeters such as Resolve on board XRISM (XRISM Science Team 2020) and *Athena*/X-IFU (Barret et al. 2016) will be able to measure the X-ray spectrum with unprecedented energy resolution, letting us measure the outflow velocity of these obscurers with much higher accuracy and allowing us to observe the full range of absorbers in AGN.

Acknowledgements. We thank the referee for improving the paper with useful comments. We acknowledge financial contribution from the agreement ASI-INAF n.2017-14-H.0. EP acknowledges support from PRIN MIUR project "Black Hole winds and the Baryon Life Cycle of Galaxies: the stone-guest at the galaxy evolution supper", contract n. 2017PH3WAT. MG acknowledges partial support by NASA *Chandra* GO8-19104X/GO9-20114X and HST GO-15890.020-A grants. AT acknowledges the financial support from FONDECYT Postdoctorado for the project n. 3190213. We acknowledge the use of public data from the *Swift* data archive. This research has made use of data and software provided by the High Energy Astrophysics Science Archive Research Center (HEASARC), which is a service of the Astrophysics Science Division at NASA/GSFC and the High Energy Astrophysics Division of the Smithsonian Astrophysical Observatory.

References

Arnaud, K. A. 1996, in Astronomical Data Analysis Software and Systems V, eds. G. H. Jacoby, & J. Barnes, ASP Conf. Ser., 101, 17
Ashton, C. E., Page, M. J., Blustin, A. J., et al. 2004, MNRAS, 355, 73
Ballo, L., Severgnini, P., Braito, V., et al. 2015, A&A, 581, A87
Barret, D., Lam Trong, T., den Herder, J. W., et al. 2016, in Proc. SPIE, SPIE Conf. Ser., 9905, 99052F
Bentz, M. C., Peterson, B. M., Netzer, H., Pogge, R. W., & Vestergaard, M. 2009, ApJ, 697, 160
Blustin, A. J., Page, M. J., Fuerst, S. V., Branduardi-Raymont, G., & Ashton, C. E. 2005, A&A, 431, 111
Braito, V., Reeves, J. N., Dewangan, G. C., et al. 2007, ApJ, 670, 978
Braito, V., Reeves, J. N., Gofford, J., et al. 2014, ApJ, 795, 87
Chartas, G., Brandt, W. N., Gallagher, S. C., & Garmire, G. P. 2002, ApJ, 579, 169
Chiaraluce, E., Vagnetti, F., Tombesi, F., & Paolillo, M. 2018, A&A, 619, A95
Cicone, C., Maiolino, R., Sturm, E., et al. 2014, A&A, 562, A21
Cicone, C., Brusa, M., Ramos Almeida, C., et al. 2018, Nat. Astron., 2, 176
Corral, A., Della Ceca, R., Caccianiga, A., et al. 2011, A&A, 530, A42
Crenshaw, D. M., & Kraemer, S. B. 2012, ApJ, 753, 75
Ferrarese, L., & Merritt, D. 2000, ApJ, 539, L9
Fiore, F., Feruglio, C., Shankar, F., et al. 2017, A&A, 601, A143
Gaspari, M., & Sądowski, A. 2017, ApJ, 837, 149
Gaspari, M., Ruszkowski, M., & Oh, S. P. 2013, MNRAS, 432, 3401
Gaspari, M., Temi, P., & Brighenti, F. 2017, MNRAS, 466, 677
Gaspari, M., Eckert, D., Ettori, S., et al. 2019, ApJ, 884, 169
Gaspari, M., Tombesi, F., & Cappi, M. 2020, Nat. Astron., 4, 10
Gehrels, N., Chincarini, G., Giommi, P., et al. 2004, ApJ, 611, 1005
George, I. M., Nandra, K., Laor, A., et al. 1997, ApJ, 491, 508
Gibson, R. R., Brandt, W. N., Gallagher, S. C., & Schneider, D. P. 2009, ApJ, 696, 924
Gofford, J., Reeves, J. N., Tombesi, F., et al. 2013, MNRAS, 430, 60
Güver, T., & Özel, F. 2009, MNRAS, 400, 2050
Halpern, J. P. 1984, ApJ, 281, 90
Häring, N., & Rix, H.-W. 2004, ApJ, 604, L89
Harrison, C. M., Alexander, D. M., Mullaney, J. R., & Swinbank, A. M. 2014, MNRAS, 441, 3306
Hewett, P. C., & Wild, V. 2010, MNRAS, 405, 2302
HI4PI Collaboration (Ben Bekhti, N., et al.) 2016, A&A, 594, A116
Jansen, F., Lumb, D., Altieri, B., et al. 2001, A&A, 365, L1
Kaastra, J. S. 2017, A&A, 605, A51
Kaastra, J. S., Kriss, G. A., Cappi, M., et al. 2014, Science, 345, 64
King, A., & Pounds, K. 2015, ARA&A, 53, 115
Laha, S., Guainazzi, M., Dewangan, G. C., Chakravorty, S., & Kembhavi, A. K. 2014, MNRAS, 441, 2613
Laha, S., Reynolds, C. S., Reeves, J., et al. 2021, Nat. Astron., 5, 13
Longinotti, A. L., Krongold, Y., Guainazzi, M., et al. 2015, ApJ, 813, L39
Luminari, A., Nicastro, F., Elvis, M., et al. 2021, A&A, 646, A111
Lusso, E., & Risaliti, G. 2016, ApJ, 819, 154
Markowitz, A. G., Krumpe, M., & Nikutta, R. 2014, MNRAS, 439, 1403
Mathur, S., Wilkes, B., & Elvis, M. 1998, ApJ, 503, L23
Matzeu, G. A., Reeves, J. N., Nardini, E., et al. 2016, MNRAS, 458, 1311
Matzeu, G. A., Reeves, J. N., Braito, V., et al. 2017, MNRAS, 472, L15
McKernan, B., Yaqoob, T., & Reynolds, C. S. 2007, MNRAS, 379, 1359
Mehdipour, M., Kaastra, J. S., Kriss, G. A., et al. 2017, A&A, 607, A28
Meidinger, N., Nandra, K., Plattner, M., et al. 2015, J. Astron. Telescopes Instrum. Syst., 1, 014006
Merloni, A., Predehl, P., Becker, W., et al. 2012, ArXiv e-prints [arXiv:1209.3114]
Middei, R., Tombesi, F., Vagnetti, F., et al. 2020, A&A, 635, A18
Nardini, E., Reeves, J. N., Gofford, J., et al. 2015, Science, 347, 860
Page, M. J., Brindle, C., Talavera, A., et al. 2012, MNRAS, 426, 903
Piconcelli, E., Jimenez-Bailón, E., Guainazzi, M., et al. 2005, A&A, 432, 15
Pounds, K. A., King, A. R., Page, K. L., & O'Brien, P. T. 2003a, MNRAS, 346, 1025
Pounds, K. A., Reeves, J. N., King, A. R., et al. 2003b, MNRAS, 345, 705
Pounds, K. A., Lobban, A., Reeves, J. N., Vaughan, S., & Costa, M. 2016, MNRAS, 459, 4389
Pu, X., Luo, B., Brandt, W. N., et al. 2020, ApJ, 900, 141
Reeves, J., Done, C., Pounds, K., et al. 2008, MNRAS, 385, L108
Reeves, J. N., Braito, V., Nardini, E., et al. 2018, ApJ, 854, L8
Reeves, J. N., Braito, V., Chartas, G., et al. 2020, ApJ, 895, 37
Richards, G. T., Lacy, M., Storrie-Lombardi, L. J., et al. 2006, ApJS, 166, 470
Risaliti, G., Elvis, M., & Nicastro, F. 2002, ApJ, 571, 234
Rose, T., Edge, A. C., Combes, F., et al. 2019, MNRAS, 489, 349
Serafinelli, R., Vagnetti, F., & Middei, R. 2017, A&A, 600, A101
Serafinelli, R., Tombesi, F., Vagnetti, F., et al. 2019, A&A, 627, A121
Severgnini, P., Ballo, L., Braito, V., et al. 2015, MNRAS, 453, 3611
Shen, Y., Richards, G. T., Strauss, M. A., et al. 2011, ApJS, 194, 45
Tombesi, F., Cappi, M., Reeves, J. N., et al. 2010, A&A, 521, A57
Tombesi, F., Cappi, M., Reeves, J. N., et al. 2013, MNRAS, 430, 1102
Tombesi, F., Meléndez, M., Veilleux, S., et al. 2015, Nature, 519, 436
Tremblay, G. R., Combes, F., Oonk, J. B. R., et al. 2018, ApJ, 865, 13
Turner, T. J., Nandra, K., Turcan, D., & George, I. M. 2001, in X-ray Astronomy: Stellar Endpoints, AGN, and the Diffuse X-ray Background, eds. N. E. White, G. Malaguti, & G. G. C. Palumbo, AIP Conf. Ser., 599, 991
Vagnetti, F., Turriziani, S., Trevese, D., & Antonucci, M. 2010, A&A, 519, A17
Vietri, G., Piconcelli, E., Bischetti, M., et al. 2018, A&A, 617, A81
Vignali, C., Brandt, W. N., & Schneider, D. P. 2003, AJ, 125, 433
XRISM Science Team 2020, ArXiv e-prints [arXiv:2003.04962]
Yoneyama, T., Noda, H., Hanaoka, M., et al. 2020, in Space Telescopes and Instrumentation 2020: Ultraviolet to Gamma Ray, eds. J. W. A. den Herder, S. Nikzad, K. Nakazawa, et al., International Society for Optics and Photonics (SPIE), 11444, 315
Zhang, S., Santangelo, A., Feroci, M., et al. 2019, Sci. China Phys. Mech. Astron., 62, 29502